Research Article

A plastic FeNi-based bulk metallic glass and its deformation behavior

Jing Zhou [a], Qianqian Wang [a], Qiaoshi Zeng [a], Kuibo Yin [b], Anding Wang [c], Junhua Luan [c], Litao Sun [b], Baolong Shen [a,d,*]

[a] School of Materials Science and Engineering, Jiangsu Key Laboratory for Advanced Metallic Materials, Southeast University, Nanjing, 211189, China
[b] SEU-FEI Nano-Pico Center, Key Laboratory of MEMS of Ministry of Education, Southeast University, Nanjing, 210096, China
[c] Center for Advanced Structural Materials, Department of Mechanical and Biomedical Engineering, College of Science and Engineering, City University of Hong Kong, Kowloon, Hong Kong, China
[d] Institute of Massive Amorphous Metal Science, China University of Mining and Technology, Xuzhou, 221116, China

ARTICLE INFO

ABSTRACT

The strength and plasticity of $Fe_{39}Ni_{39}B_{12.82}Si_{2.75}Nb_{2.3}P_{4.13}$ bulk metallic glass (BMG) are improved simultaneously by modulating atomic-scale structure through fluxing treatment. The compression strength increases from 3074 to 4220 MPa, and the plastic strain is enlarged from 10.7 % to more than 50 %. The increased mechanical properties of the fluxed FeNiBSiNbP BMG originate from the optimization of atomic-scale structure. More icosahedral-like clusters (ILCs) and crystal-like clusters (CLCs) are found in this FeNi-based BMG with fluxing treatment, and the ILCs are usually surrounded by CLCs. Furthermore, phase separation and a sandwich-like heterogeneous structure of SB are also observed during deformation, indicating the multiscale deformation mechanism and a stable shear-band evolution. The unique "ILC surrounded by CLCs" structure and phase separation lead to a stable plastic deformation process with strong interactions of multiple shear bands, thereby the improved plasticity and strength. This work provides useful guidelines to develop strong and plastic Fe-based BMGs from a structural aspect.

© 2020 Published by Elsevier Ltd on behalf of The editorial office of Journal of Materials Science & Technology.

1. Introduction

Bulk metallic glasses (BMGs) have attracted great research attention due to their superhigh strength, high elastic limit, as well as excellent wear and corrosion resistance [1]. Nevertheless, the deformation of BMGs is usually localized in nanoscale narrow regions termed as shear bands (SBs), resulting in the poor deformability of most BMGs at room temperature, which severely limits their potential application as engineering structural materials. In the past decades, the plasticity of BMGs has been improved by alloying elements that have large Poisson's ratio [2,3], precipitation of ductile phase in BMG matrix [4,5], or applying extrinsic enhancing approaches (e.g., imprinting [6], thermal cycling [7], and high-pressure torsion [8], etc.). However, the enhanced plasticity of BMGs is usually traded off with a loss in strength. Especially for Fe-based BMGs, the ductile alloy systems with a plastic strain of more than 10 % exhibit relatively low yield strength [9–12], such

as the $Fe_{50}Ni_{30}P_{13}C_7$ BMG with plastic strain over 50 % exhibits the lowest yield strength of 2250 MPa among Fe-based BMG family [10,11]. Thus, the desired combination of superior plasticity and high strength of Fe-based BMGs remains a challenge and has been a research focus.

Recent studies show that modulation of the atomic-scale structure of some BMGs through compositional design is effective to simultaneously enhance the plasticity and strength. In $Cu_{50}Zr_{50}$ BMG, the strength of BMG was improved by adding Al element because of the formation of more icosahedral medium-range orders, and the uniform distribution of these clusters also improved the plasticity [13]. Simultaneous improvement in plasticity and strength was also achieved in $Cu_{46}Zr_{46}Ag_8$ BMG by introducing atomic-scale heterogeneities as Ag and Cu have a positive mixing enthalpy [14]. Similarly, a ductile $(Co_{0.7}Fe_{0.2}Ni_{0.1})_{67.7}B_{21.9}Si_{5.1}Nb_5Cu_{0.3}$ BMG with superhigh strength was developed by the formation of crystal-like ordering clusters [15]. However, this method can be used only for specific alloy systems, where the desired atomic-scale structure can be obtained by compositional modulation. It should be noted that the atomic-scale structure of BMGs with a certain composition can change with the processing techniques. For instance, the molten liquid can be undercooled far below the melt-

* Corresponding author at: School of Materials Science and Engineering, Jiangsu Key Laboratory for Advanced Metallic Materials, Southeast University, Nanjing, 211189, China.

E-mail address: blshen@seu.edu.cn (B. Shen).

ing temperature through fluxing treatment, which may induce different atomic clusters and thus change the mechanical properties. Using this method, the ductile $Pt_{57.7}Cu_{14.7}Ni_{5.3}P_{22.5}$ [16] and "liquid-like" $Pt_{74.7}Cu_{1.5}Ag_{0.3}P_{18}B_4Si_{1.5}$ [17] BMGs with the plastic strain of more than 20 % under compressive loading were developed. Subsequently, a novel $Pd_{79}Ag_{3.5}P_6Si_{9.5}Ge_2$ BMG with fluxing treatment was successfully prepared, which exhibits the highest fracture toughness of 200 MPa m$^{1/2}$ among all BMGs and rivals the best known crystalline alloys in damage tolerance [18]. Recently, a $Fe_{50}Ni_{30}P_{13}C_7$ BMG with unprecedented plastic strain up to 50 % was also developed using the fluxing technique [10,11]. Inspired by these works, we aim to develop plastic Fe-based BMGs with high strength through optimization of atomic-scale structure induced by fluxing treatment in this study.

Furthermore, the reason for the improved mechanical properties of BMGs through fluxing treatment remains unidentified. Chen et al. suggested that fluxing treatment is likely to change the atomic-scale structure of BMGs and thus leads to the significant enhancement of plasticity in $Pd_{40}Ni_{40}Si_4P_{16}$ BMG [19,20]. Granata et al. proposed that the fluxing induced improvement of the plasticity of BMGs is attributed to the reduced amount of oxide impurities [21,22]. Johnson et al. revealed that fluxing bring to the compositional modification [23], which is the reason for the change of mechanical properties of fluxed BMGs [24]. Very recently, Eckert et al. verified that the fluxing induced improvement of plasticity in a Fe-based BMG can be attributed to the formation of nanocrystal in the amorphous matrix [11]. These debates indicate that further in-depth investigations for the mechanism of fluxing effects in BMGs still need to be pursued.

Nevertheless, a major challenge is to clarify the atomic-scale structural differences and to establish a causal link between local structure and macroscopic mechanical properties in BMGs. In this regard, due to the SBs are the carriers of deformation in BMGs, the structural evolution of SBs during deformation is believed to be a key element to originate the effect of fluxing treatment on mechanical properties of Fe-based BMGs. The initiation, propagation and evolution of SBs in Zr-, Pd-based BMGs have been qualitatively and quantitatively well studied [25–28], whereas the investigation of SBs in Fe-based BMGs has rarely been reported. Therefore, it is meaningful to reveal the origin of fluxing effects in the enhanced mechanical properties of Fe-based BMGs from a perspective of SB evolution, which is another key point of this work.

In this study, the $Fe_{39}Ni_{39}B_{12.82}Si_{2.75}Nb_{2.3}P_{4.13}$ BMG with high strength of 3300 MPa, large plasticity of 9.8 % and excellent soft magnetic properties [29] was selected as the base alloy for fluxing treatment to further optimize the mechanical properties. As a result, the fluxed $Fe_{39}Ni_{39}B_{12.82}Si_{2.75}Nb_{2.3}P_{4.13}$ BMG exhibiting large plastic strain exceeding 50 % and superhigh compression strength of 4220 MPa was successfully developed. Moreover, detailed investigations were carried out to study the effects of fluxing treatment on the mechanical properties of this FeNi-based BMG from an atomic-structure perspective. The characteristics of atomic-scale structure for fluxed and unfluxed FeNi-based BMGs were investigated by three-dimensional atom probe tomography (3D-APT), synchrotron X-ray diffraction (XRD) and high-resolution transmission electron microscopy (HRTEM). Besides, the structural origin of enhanced plasticity and strength of fluxed $Fe_{39}Ni_{39}B_{12.82}Si_{2.75}Nb_{2.3}P_{4.13}$ BMG was also discussed based on the evolution of SBs under compression loading.

2. Experimental section

2.1. Sample preparation and mechanical property test

Master alloy ingots with nominal composition of $Fe_{39}Ni_{39}B_{12.82}Si_{2.75}Nb_{2.3}P_{4.13}$ were prepared by induction melting a mixture of constituent elements with a purity of above 99.9 %. Two different modifications of $Fe_{39}Ni_{39}B_{12.82}Si_{2.75}Nb_{2.3}P_{4.13}$ BMGs were performed and labeled as unfluxed sample and fluxed sample, respectively. For unfluxed sample, the FeNi-based BMG rod were produced by copper mold casting method. For fluxed sample, the alloy ingot were fluxed in a fluxing agent composed of B_2O_3 and CaO with a mass ratio of 3:1 at 1500 K for several hours under a vacuum of ~10 Pa. After fluxing treatment, the rod sample was produced by copper mold casting method. The plastic strain (ε_p) and compression strength (σ_c) were measured at room temperature by compressive measurements with a Sans 5305 testing machine at a strain rate of 5×10^{-4} s^{-1}. The unfluxed and fluxed samples were cut from the as-cast glassy rods with aspect ratio (Height/Diameter, H/D) = 2:1 and 1.5:1 (1 mm in diameter).

2.2. Structure characterization

The morphology of deformed and fractured surface was observed by scanning electron microscope (SEM, Sirion 200, FEI). Needle-shaped specimens required for APT were fabricated by lift-outs and annular milled in a FEI Scios focused ion beam/scanning electron microscope (FIB/SEM). The APT characterizations were performed in a local electrode atom probe (CAMEACA LEAP 5000 XR). The specimens were analyzed at 60 K in laser mode, a pulse repetition rate of 200 kHz, a pulse energy of 10 pJ, and an evaporation detection rate of 0.3 % atom per pulse. Imago Visualization and Analysis Software (IVAS) version 3.8 was used for creating the 3D reconstructions and data analysis. The atomic-scale structure of unfluxed and fluxed FeNi-based BMGs was tested by synchrotron XRD using the beam line 11-IDC in the Advanced Photon Source, Argonne National Laboratory, USA. The photon energy was 105.1 keV corresponding to an X-ray wavelength of 0.11798 Å and the beam size was 0.5×0.5 mm^2. The X-ray attenuation length of the samples at 105.1 keV is ~2.5 mm. The samples were sandwiched between two layers of Kapton tape to increase the sample thickness (in this case ~200 mm). A Perkin Elmer area detector was set at a distance of 690.7 mm and CeO_2 was used as the calibration material. The exposure time was 90 s for each sample and the background scattering from the air and the two layers of Kapton tape. The resultant 2D image files were integrated using the Fit2D program [30] to obtain 1D intensity distributions as a function of the wavevector Q, from which the S(Q) and the G(r) were derived with the PDFgetX2 program [31]. Further HRTEM observations of as-cast and deformed samples were carried out on an aberration-corrected FEI Titan 80/300 microscope. The HRTEM samples were prepared by the ion milling method (Gatan Inc., PIPS-M691) under liquid nitrogen cooling conditions.

3. Results

3.1. Excellent mechanical properties

Fig. 1 shows the true stress-strain curves of unfluxed and fluxed $Fe_{39}Ni_{39}B_{12.82}Si_{2.75}Nb_{2.3}P_{4.13}$ BMG samples with an aspect ratios of H/D = 2/1. As shown in the figure, with the fluxing treatment, the ε_p and σ_c increase dramatically from 9.8–17.2% and 3050–4220

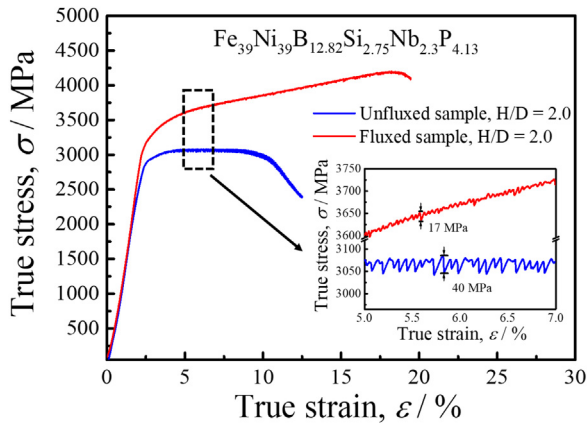**Fig. 1.** The true stress-strain curves at room temperature of the unfluxed and fluxed $Fe_{39}Ni_{39}B_{12.82}Si_{2.75}Nb_{2.3}P_{4.13}$ BMG samples with an aspect ratio of H/D = 2:1. The inset is the enlarged regions pointed by black rectangle.

MPa, respectively, and the fluxed sample shows strain-hardening characteristics. The inset shows the enlarged stress-strain curves during the steady-state deformation region. It is clearly seen that the serration pattern becomes more complex, and the maximum serration size decreases from 40 to 17 MPa with fluxing treatment. Furthermore, the magnitude of stress drop was extracted from the stress-strain curves and these data were statistically analysed. Fig. 2a and b show the statistic stress drop ($\triangle\sigma$) as a function of strain of unfluxed and fluxed samples, respectively. As shown in the figures, the unfluxed sample exhibits the larger average serration size ($\bar{\triangle\sigma}$) of 20.5 MPa, and a high proportion of serrations at large size (Fig. 2a), by contrast, the fluxed sample shows much smaller $\bar{\triangle\sigma}$ of 3.83 MPa, and a high proportion of serration at a small size (Fig. 2b). Previous studies show that the size and number of serrations could represent the sliding distance and number of SBs activated in BMG sample [32]. Thus, the larger number of serrations with smaller size of fluxed sample indicates a more stable deformation process with the formation of multiple SBs [33], resulting in the extensive plasticity observed in the fluxed FeNi-based BMG. In addition, the increasing rate of serration size ($\triangle\sigma_{max}/\triangle\varepsilon$) decreases from 6.85 to 1.82 MPa/% with fluxing treatment, suggesting a higher frequency of shear-band nucleation and a higher degree of inhomogeneity [32,34].

Fig. 3 shows SEM images of lateral and fracture surfaces of unfluxed and fluxed samples after compressive failure. A distinct primary SB, which is ~45° to the loading direction, can be observed on the surface of unfluxed sample after deformation (Fig. 3a), and only a handful of secondary SBs branching are visible around the primary SB (Fig. 3c, enlarged region A in Fig. 3a). On the contrary, a significant extension of stable shearing by forming a primary SB and high density of well-developed secondary SBs can be observed on the lateral surface of the fluxed sample (Fig. 3b). The primary SB is inclined by ~45° to the loading direction, while the shear slips on the secondary shear planes are ~60° to the loading direction, and the strong interactions between them result in the formation of serrated SBs (Fig. 3d, enlarged region B in Fig. 3b). The highly branched and deflected SBs accounting for many multiple SBs formation accommodate the large plastic strain of fluxed sample [35], instead of rapid propagation along the primary SBs. Furthermore, the fracture surface of the fluxed sample was examined, and robust plastic flow patterns on the fracture surface can be observed, as shown in Fig. 3e. It is worth to mention that there are two distinct fracture morphologies in the main shear plane. In Fig. 3e, the fracture surface shows well-developed vein patterns with an average scale of about 20 μm, and some protruding veins have fallen over. Also, many spheroidal particles are found on the fracture surface,
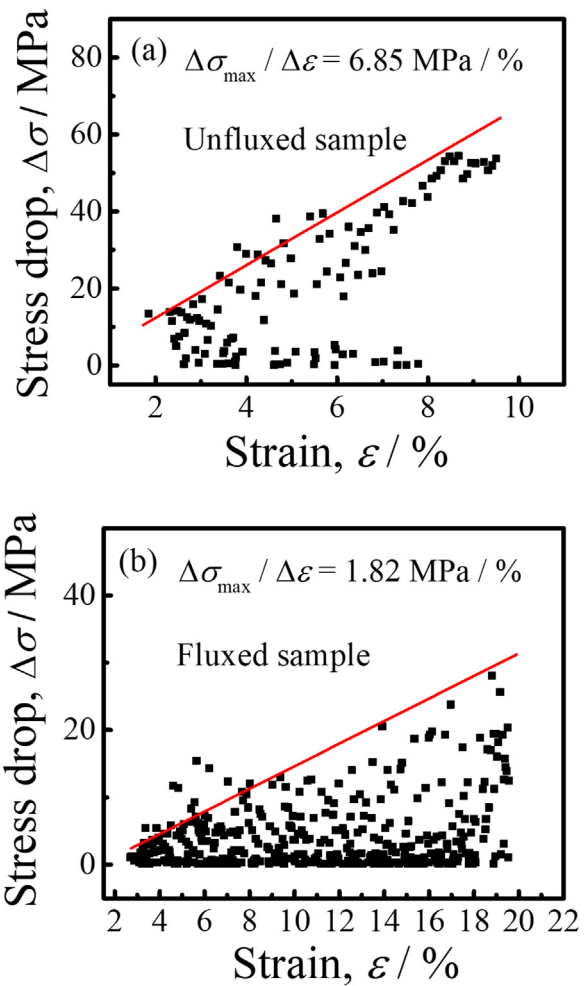

Fig. 2. A statistic results of stress drop ($\triangle\sigma$) for (a) Unfluxed and (b) fluxed $Fe_{39}Ni_{39}B_{12.82}Si_{2.75}Nb_{2.3}P_{4.13}$ BMG samples, the increasing rate of serration size ($\triangle\sigma_{max}/\triangle\varepsilon$) is the slop of the red line.

confirming the appearance of melting liquid drops during fracturing. These features mean the local viscous flow of metallic glass and reveal the solidification of melted liquid flow with the fast cooling process, which can only occur in the BMG samples with good ductility [11,12]. In Fig. 3f, finger-like vein patterns can be observed, which are frequently seen on the tension surfaces of BMG samples, suggesting the local tension stress state at the fractured moment, which is frequently seen on the tension surface of BMG samples [36]. It has been reported that this tension stress state is attributed to the inclination of the test sample induced by the superfast shearing at the moment of compression fracture [36], which is more likely to occur in Fe-based BMGs with superhigh strength.

To obtain the intrinsic shear resistance of these FeNi-based BMGs, the samples with an aspect ratio of 1.5 were used in compression tests to avoid the inclination at the fractured moment. Fig. 4a shows the true stress-strain curves of unfluxed and fluxed $Fe_{39}Ni_{39}B_{12.82}Si_{2.75}Nb_{2.3}P_{4.13}$ BMG samples with an aspect ratio of 1.5. As shown in the figure, the unfluxed sample exhibits similar values of ε_p (10.6 %) and σ_c (3074 MPa) compared to the unfluxed sample with an aspect ratio of 2. Surprisingly, the fluxed sample shows a very large ε_p, even exceeding 50 %, akin to the previously plastic $Fe_{50}Ni_{30}P_{13}C_7$ [10,11] and $Fe_{62}Ni_{18}P_{13}C_7$ BMGs [12]. Due to the pronounced plastic deformation, the present FeNi-based BMG rod sample was compressed into a flake-like geometry without apparent fracturing, as shown in the inset of Fig. 4a. Besides, Fig. 4b and c exhibit strong interactions of multiple SBs on the lateral sur-
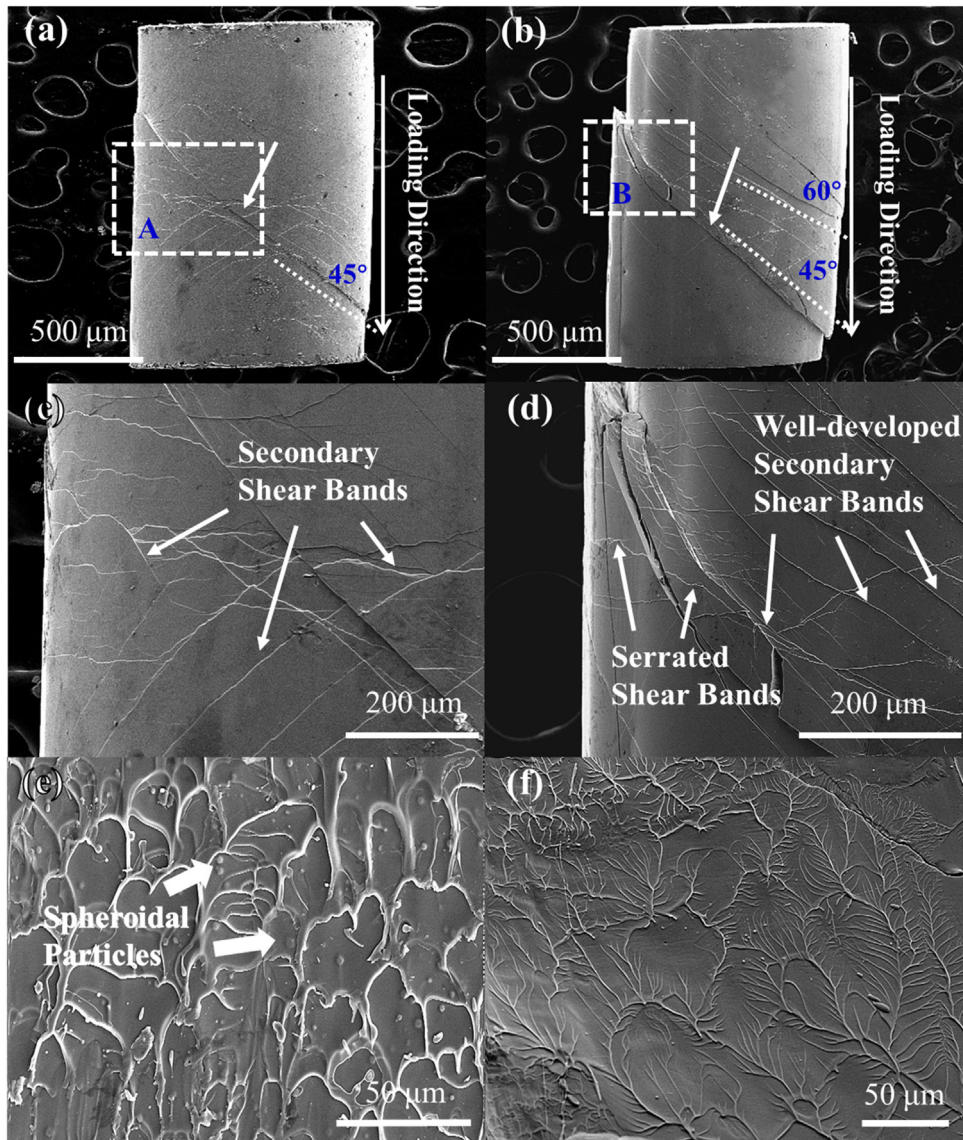
Fig. 3. SEM images of the lateral of deformed samples of (a) unfluxed and (b) fluxed $Fe_{39}Ni_{39}B_{12.82}Si_{2.75}Nb_{2.3}P_{4.13}$ BMGs, which were unloaded before failure in compression. (c) and (d) are the enlarged SEM images of region A in (a) and region B in (b), respectively. (e) and (f) are the enlarged fracture features of fluxed $Fe_{39}Ni_{39}B_{12.82}Si_{2.75}Nb_{2.3}P_{4.13}$ BMG sample after failure showing well-developed vein patterns and finger-like patterns, respectively.

face of the fluxed sample after deformation. As shown in Fig. 4b, the SBs are branched and deflected to the direction perpendicular to the loading axle, resulting in a large shift from their propagation paths, as indicated by a deflective SB angle of 70°. Meanwhile, many small ledges, branches, and kinks along the SBs are also observed in Fig. 4c, indicating the excellent resistance to the propagation of SBs. The strong interactions of multiple SBs and the appearance of vein patterns shown in Fig. 3e verify the extraordinary plasticity of fluxed $Fe_{39}Ni_{39}B_{12.82}Si_{2.75}Nb_{2.3}P_{4.13}$ BMG.

To highlight the excellent mechanical properties of this fluxed FeNi-based BMG, the ε_p and σ_c of typical Fe-based BMGs are summarized and shown in Fig. 5 [9–12,29,37–55]. It is seen that the compression strength correlates almost inversely to the plastic strain among the Fe-based BMG family (illustrated by the blue dotted curve). Among them, all the unfluxed Fe-based BMGs exhibit high σ_c over 3000 MPa, but show limited ε_p that is less than 10 %. In contrast, some fluxed Fe-based BMGs show large ε_p over 10 %, especially, the $Fe_{50}Ni_{30}P_{13}C_7$ BMG[1∘,11] exhibits extremely large ε_p up to 50 %, but the strength of these fluxed BMGs are around 2500 MPa. It seems that the Fe-based BMGs subjected to fluxing treatment

exhibits large plasticity, but relatively lower strength. Nevertheless, there is a counterexample that the fluxed $Fe_{74}Mo_6P_{13}C_7$ BMG [55] shows an enhanced plastic strain of 6% and a high strength of 3400 MPa. Thus, it is promising that the fluxing technique can improve the plasticity of Fe-based BMGs while keeping their strength. In this study, the fluxed $Fe_{39}Ni_{39}B_{12.82}Si_{2.75}Nb_{2.3}P_{4.13}$ BMG with unexpected mechanical properties of large ε_p up to 50 % and high σ_c of 4220 MPa, which is plotted as a red star in the figure, is a breakthrough of the σ_c-ε_p trade-off for the Fe-based BMG family. In the following section, the origin of the enhanced plasticity and strength for this fluxed $Fe_{39}Ni_{39}B_{12.82}Si_{2.75}Nb_{2.3}P_{4.13}$ BMG will be discussed in detail.

3.2. D-APT analysis

The 3D-APT investigation of the unfluxed and fluxed $Fe_{39}Ni_{39}B_{12.82}Si_{2.75}Nb_{2.3}P_{4.13}$ BMG samples were performed to determine whether the enhanced plasticity comes from the chemical segregation occurred during solidification, as shown in Fig. 6. The 3D-APT tip reconstructions of all elements for unfluxed
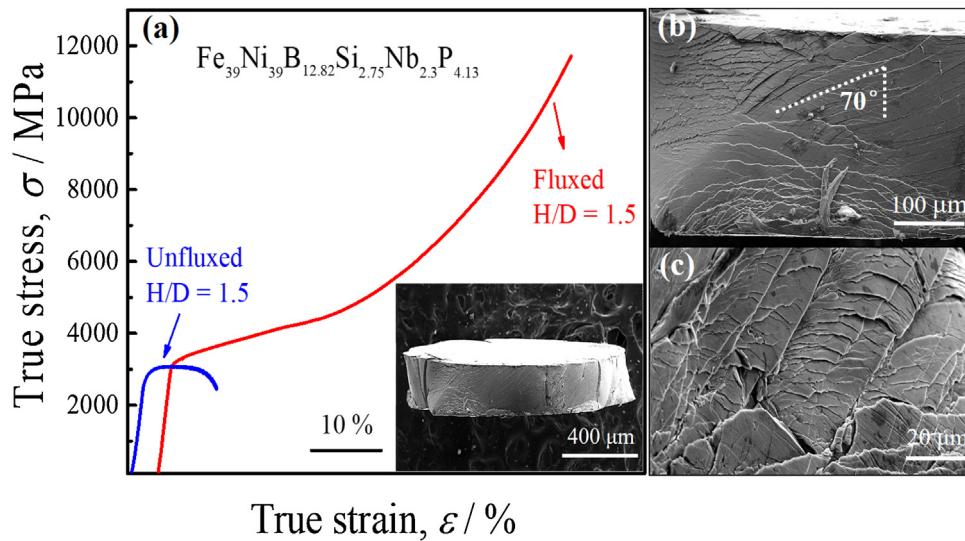
Fig. 4. (a) The true stress-strain curve of fluxed $Fe_{39}Ni_{39}B_{12.82}Si_{2.75}Nb_{2.3}P_{4.13}$ BMG samples with an aspect ratio of H/D = 1.5:1. The inset shows the sample after deformation (up to 30 % strain). (b) and (c) are SEM images of high magnification of the compressed sample in the inset of (a), showing multiple SBs. The true stress-strain curve of unfluxed sample was also shown for comparison.
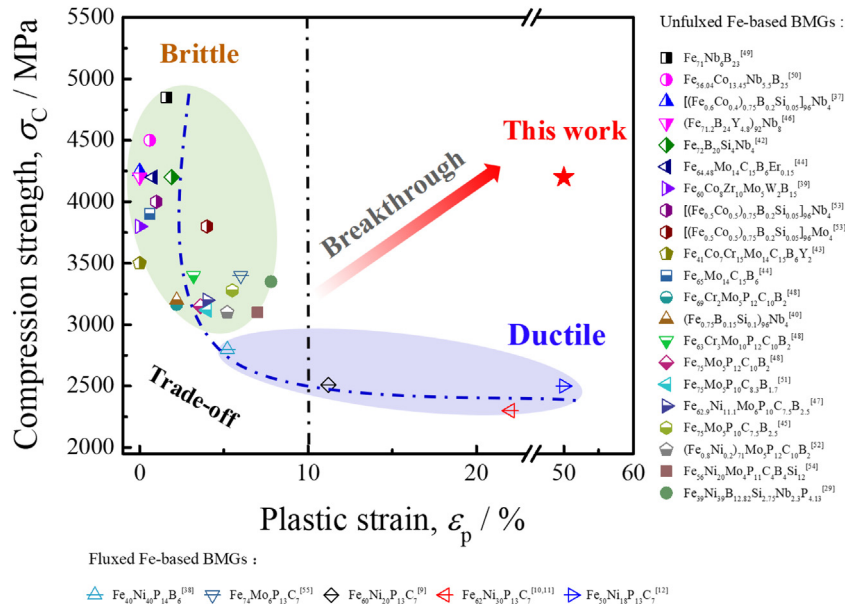

Fig. 5. The relationship between compression strength (σ_c) and plastic strain (ε_p) of the typical Fe-based BMGs at room temperature.

and fluxed samples shown in Fig. 6a reveal that no evidence of phase separation can be observed, and all the elements are homogeneously distributed without any chemical segregation. Fig. 6b and c show the corresponding statistical binomial frequency distribution analysis of the unfluxed and fluxed samples, respectively [56–58]. For both samples, the binomial curves match the curves obtained from experiments, suggesting a totally random distribution. The quality of the fit was quantified using several parameters as listed in the insets of Fig. 6b and c. Reduced χ^2 $=\Sigma(N_{obs}-N_{exp})^2/N_{exp}$ is the deviation of the measured distribution from the binomial distribution, which represents the degree of the heterogeneous distribution of sample compositions. Where N_{obs} and N_{exp} is the number of bins observed in the experimental at a certain elemental concentration and expected from a homogenous alloy with random distributions, respectively, as modeled by a binomial distribution, n_d is the number of degrees of freedom for a given ion, and μ is the normalized homogenization parameter.

The values of μ for all elements in both unfluxed and fluxed samples are close to 0, confirming the random distribution of all the elements (Fe, Ni, B, Si, Nb, P). The reduced χ^2 for Fe, Ni, B, Si, Nb, P elements of unfluxed sample are less than 4, also indicating an even distribution of all components. However, the reduced χ^2 for B, Si, Nb of fluxed sample is much higher as compared with that of the unfluxed sample. The change of reduced χ^2 leaves a hint that the atomic-scale structure of the FeNi-based BMG might be changed through fluxing treatment. Moreover, as shown in the insets of Fig. 6b and c, the fluxed sample exhibits lower content of Si element and higher content of B element than the unfluxed sample. This unexpected B enrichment and Si depletion in the fluxed BMG sample are also reported by Johnson and Löffler et al. [22,23], indicating a composition change with the fluxing treatment, which might be associated with the structural change of BMGs [19,20].
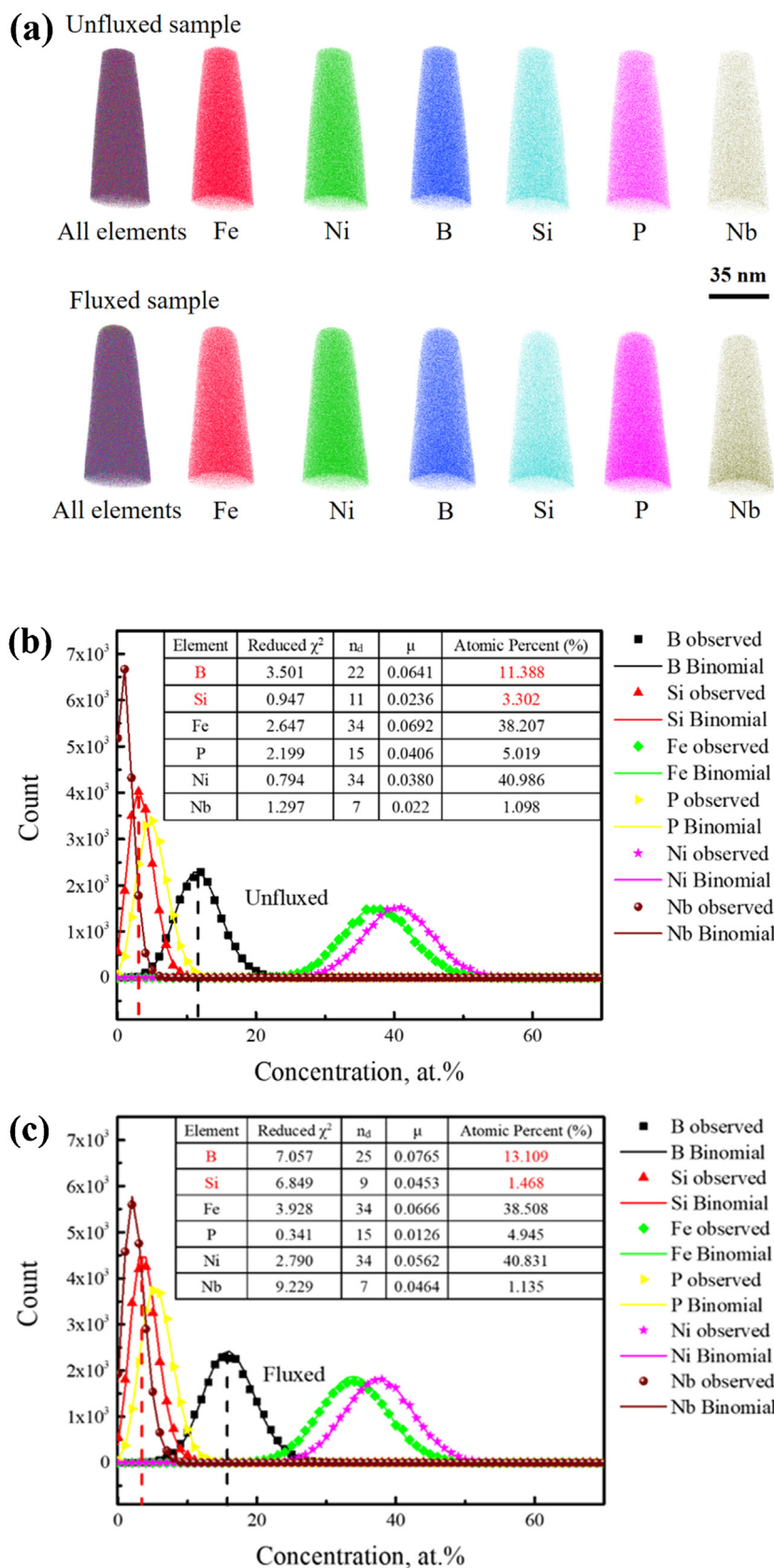
(a) Unfluxed sample

All elements   Fe   Ni   B   Si   P   Nb

35 nm

Fluxed sample

All elements   Fe   Ni   B   Si   P   Nb

(b)

Element	Reduced χ^2	n_d	μ	Atomic Percent (%)
B	3.501	22	0.0641	11.388
Si	0.947	11	0.0236	3.302
Fe	2.647	34	0.0692	38.207
P	2.199	15	0.0406	5.019
Ni	0.794	34	0.0380	40.986
Nb	1.297	7	0.022	1.098

Unfluxed

- ■ B observed
- —— B Binomial
- ▲ Si observed
- —— Si Binomial
- ◆ Fe observed
- —— Fe Binomial
- ▶ P observed
- —— P Binomial
- ★ Ni observed
- —— Ni Binomial
- ● Nb observed
- —— Nb Binomial

Count

Concentration, at.%

(c)

Element	Reduced χ^2	n_d	μ	Atomic Percent (%)
B	7.057	25	0.0765	13.109
Si	6.849	9	0.0453	1.468
Fe	3.928	34	0.0666	38.508
P	0.341	15	0.0126	4.945
Ni	2.790	34	0.0562	40.831
Nb	9.229	7	0.0464	1.135

Fluxed

- ■ B observed
- —— B Binomial
- ▲ Si observed
- —— Si Binomial
- ◆ Fe observed
- —— Fe Binomial
- ▶ P observed
- —— P Binomial
- ★ Ni observed
- —— Ni Binomial
- ● Nb observed
- —— Nb Binomial

Count

Concentration, at.%

Fig. 6. APT analysis on the unfluxed and fluxed $Fe_{39}Ni_{39}B_{12.82}Si_{2.75}Nb_{2.3}P_{4.13}$ BMG samples. (a) The atom map for corresponding Fe, Ni, B, Si, Nb, P elements distribution of unfluxed and fluxed samples. Frequency distribution analysis of the composition of (b) unfluxed and (c) fluxed samples, obtained from experimental results and the binomial simulation, respectively. Several parameters employed to assess the quality of the fit of the experimental results to the binomial simulation and the corresponding atomic percentage are listed in the inserted tables of (b) and (c).

3.3. Synchrotron XRD characterization

To further understand the origin of the dramatic changes in the mechanical response upon fluxing treatment from a structural perspective, the synchrotron XRD measurements on unfluxed and fluxed samples were carried out. Fig. 7a shows the total structural factor $S(Q)$ as a function of the scattering vector Q of fluxed and unfluxed $Fe_{39}Ni_{39}B_{12.82}Si_{2.75}Nb_{2.3}P_{4.13}$ BMG samples. It can be seen that both the samples show the typical diffuse scattering pattern of a fully glassy structure. Fig. 7b shows the enlarged region of the first peaks of $S(Q)$ with the dashed lines denoting the peak position. The first $S(Q)$ peaks are located at 3.11 Å^{-1} for unfluxed sample and 3.12 Å^{-1} for fluxed sample, respectively, and the intensity of the first $S(Q)$ peak decreases from 3.29 to 3.20 with fluxing treatment. It has been reported that both shift and broadening of the first $S(Q)$ peak indicate the structural evolution in glassy alloys in the medium-range scale [59]. Besides, no significant shift is observed for other peaks between the fluxed and unfluxed samples, and the second $S(Q)$ peaks have a shoulder in the high Q-side for both alloys, which is a common characteristic of many metallic glasses and indicates the existence of short-range ordering (SRO) [60].

The changes of atomic-scale structure for unfluxed and fluxed $Fe_{39}Ni_{39}B_{12.82}Si_{2.75}Nb_{2.3}P_{4.13}$ BMG samples were also investigated in real space, through analyzing the reduced-pair distribution $G(r)$ with each peak defined as r_i (i = 1, 2, 3, etc.), which is defined as $G(r) = 4\pi r\rho_0(g(r)-1)$, where r is the distance, ρ_0 is the average number density, and $g(r)$ is pair distribution function (Fig. 7c). The $g(r)$ tends to 0 at small r because atoms cannot overlap, which forces $G(r)$ to behave as $-4\pi r\rho_0$ as $r \to 0$. At low r, the slope of $G(r)$ is proportional to the average number density of the material. Here, the slope of $G(r)$ for both BMGs at r < 2 Å are almost the same (Fig. 7d), indicating the same density of these two alloys, in another word, the same free volume stored in unfluxed and fluxed samples. Fig. 7e shows the enlarged region of $G(r)$ focused on the peaks corresponding to the first nearest neighbor shell of atoms (r_1), which is important to understand the change in SRO. It is shown that the position of r_1 remains at 2.56 Å for both samples, while the intensity increases from 5.124 for the unfluxed sample to 5.185 for the fluxed sample, causing the full width at half maximum (FWHM) of the first peak decreases from 0.5348 to 0.5327, indicating more pronounced topological ordering on short-range scale in the fluxed sample.

On the other hand, the peaks of $G(r)$ locating beyond the first peak also change considerably with fluxing treatment, the enlarged region from q_2 to q_8 peaks are shown in Fig. 7f. Table 1 summarizes the peak positions of these medium-range order (MRO) peaks of unfluxed and fluxed samples. It is shown that all peaks slightly shift towards smaller r value (ranging from 0.03 to 0.33 %) and the intensity decreases by $\sim$ 3.10 %–16.3 %, which corresponds to fewer atoms at certain set radial distances and more atoms distributed randomly. These results indicate that fluxing treatment for this FeNi-based BMG leads to a decrease in coordination number and MRO, which is consistent with the analyses of $S(Q)$ curves.

3.4. HRTEM observation of atomic-scale structure

To gain insights into the fluxing-induced atomic-scale structural change revealed by the synchrotron XRD measurements, the HRTEM observations were also carried out. Fig. 8a and b show the HRTEM image and Fast-Fourier-Transformation (FFT) pattern of unfluxed and fluxed $Fe_{39}Ni_{39}B_{12.82}Si_{2.75}Nb_{2.3}P_{4.13}$ BMG samples, respectively. Both samples exhibit the amorphous structure of maze-like patterns, and the FFT patterns show typical amorphous halo rings. Nevertheless, as mentioned above, the atomic-scale ordering is different between them. To reveal such a change in the local atomic structure, the enlarged region of the selected areas (white squares in Fig. 8a and b) of the corresponding HRTEM images

are shown in Fig. 8c and d, respectively, and the insets show the FFT patterns taken from the two square areas. As seen in Fig. 8c and d, both the samples contain local icosahedral-like clusters (ILC) [61–63] (marked by yellow circles) and crystal-like [11,64,65] clusters (CLC) (marked by the red dash lines), both of which are typically of 0.5–1 nm in size and have been identified in various metallic glasses. FFT patterns showing bright spots on the broad halo indicate the presence of the crystal-like regions. The average lattice fringes are around 2.05 ± 0.05 Å, which may correspond to an FCC metallic crystalline phase (FCC-FeNi with bulk (111) lattice spacing of 2.08 Å) [66]. However, fewer FCC-FeNi nanocrystals and icosahedral-like atomic clusters are observed in the unfluxed sample than in the fluxed sample. Besides, the icosahedral-like atomic clusters aggregate with each other in the unfluxed sample, while homogenously distribute throughout the amorphous matrix and surrounded by several nanocrystals in the fluxed sample. This unique atomic-scale structure in the fluxed sample is marked by green rectangles in Fig. 8d, and the enlarged image of region A is shown in Fig. 8e for more clarity. Moreover, the corresponding image for auto-correlation analysis by using custom Digital Micrograph scripts based on the evaluation of the local autocorrelation function is shown in Fig. 8f, in which the dimension of each cell is 0.812×0.812 nm^2. It can be seen that a five-fold symmetry pattern (the middle cell with yellow frame) is surrounded by several ordered patterns of the crystal structure (the cells with green frame) and disordered patterns of the amorphous structure (the cells with brown frame). These results further confirm the existence of the unique "ILC surrounded by CLCs" atomic-scale structure in the fluxed FeNi-based BMGs.

This auto-correlation analysis was also used to quantitatively study the areal fraction of MRO in unfluxed and fluxed samples. Fig. 9a and b show the segmentations of the HRTEM images for the unfluxed and fluxed $Fe_{39}Ni_{39}B_{12.82}Si_{2.75}Nb_{2.3}P_{4.13}$ BMG samples, respectively. Here, the dimension of each cell is 1.915×1.915 nm^2, which is close to the size of MRO. Autocorrelation of these cells is characterized into two categories, which are the fringes and maze-like patterns. The fringe corresponds to the crystal-like structure, while the maze-like pattern corresponds to the disordering structure. For example, the cell locating in the 1 st row and 2nd column in Fig. 9a is characterized by crystal-like symmetry in its FFT pattern [64] and exhibits fringes in the 2D auto-correlation map. Therefore, it was chosen as a reference pattern to study the local ordering in the present case. In this regard, all the sub-images in the rest of the square cells were considered to be ordered if their 2D auto-correlation patterns display a clearer fringe than the reference one [67,68]. According to the above method, all cells in the HRTEM images were analyzed. As a result, the fraction of the area of the MRO is 25 % in the unfluxed sample, but that decreases to 21 % in the fluxed sample as shown in Fig. 9b, indicating the reduced structural ordering in the medium-range scale, which is also consistent with the results of synchrotron XRD measurements shown in Fig. 7f. Based on these results, more CLCs and ILCs in the fluxed sample bring to the increase of short-range heterogeneity. Meanwhile, the uniform distribution of the CLCs and ILCs results in a high disordering degree in the medium-range.

The further HRTEM measurement of the fluxed sample compressed to 30 % plastic strain was examined to identify the structure change of the unique short-to-middle-range order and a more particular knowledge of the mechanism of remarkable plasticity enhancement. As shown in Fig. 10a, a few unparallel SBs with several micrometres long are observed (marked by red and green lines). At the central intersection area (circled), a complex plastic deformation zone is formed, indicating the strong interactions of multiple SBs. Besides, it is worth mentioning that numerous bright nanospheres with dimensions of several nanometers are observed in the SB affected zone. From the FFT pattern in the inset
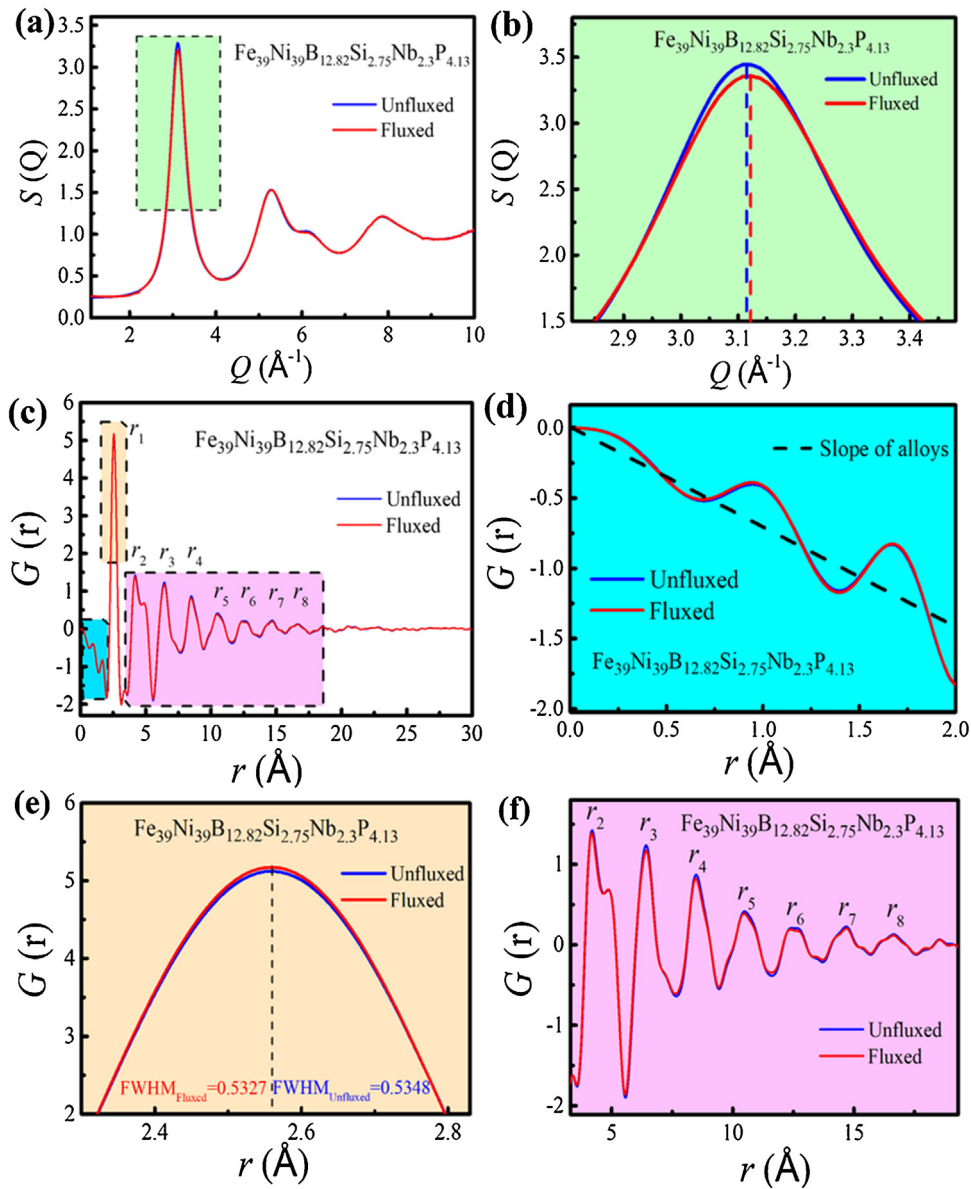
Fig. 7. The synchrotron XRD results of unfluxed and fluxed $Fe_{39}Ni_{39}B_{12.82}Si_{2.75}P_{4.13}Nb_{2.3}$ BMG samples. (a) Total structure factor $S(Q)$, (b) enlarged region on the first peaks of $S(Q)$ shown in (a) with the dashed lines denoting the peak positions, (c) reduced pair distribution function $G(r)$, (d) enlarged region on the $G(r)$ function shown in (c) at $r \le$ 2.0 Å with dashed lines denoting the slope of the curve in this low-r region, (e) enlarged region on the first nearest neighbor peaks of $G(r)$ function shown in (c), (f) enlarged region from q_2 to q_8 peaks of $G(r)$ function shown in (c).

Table 1
Analysis of MRO peaks in $G(r)$.

Peak	Peak location in $G(r)$			Peak intensity in $G(r)$		
	Unfluxed	Fluxed	Change	Unfluxed	Fluxed	Change
r_2	4.191	4.177	0.33 %	1.419	1.375	3.10 %
r_3	6.425	6.426	0.01%	1.243	1.169	6.00 %
r_4	8.491	8.470	0.25 %	0.867	0.820	5.42 %
r_5	10.490	10.462	0.27%	0.415	0.388	6.51 %
r_6	12.411	12.372	0.31%	0.208	0.174	16.3 %
r_7	14.693	14.688	0.03%	0.227	0.195	14.1 %
r_8	16.651	16.646	0.03%	0.132	0.112	15.2 %

of Fig. 10a, it can be confirmed that these nanospheres are also of glassy structure, suggesting phase separation occurred under the compression loading. For clarity, Fig. 10b shows the magnification image of SBs with a thickness of ~10 nm, as marked by red and green dash lines. Compared with the surrounding matrix, the

coarsening of nanospheres in the SB marked by red dash lines can be seen. From the FFT pattern of the selected area in the white box of Fig. 10b, it can be further confirmed that these nanospheres are fully glassy structure. However, in the other SBs marked by green dash lines, no obvious nanospheres can be found, suggesting
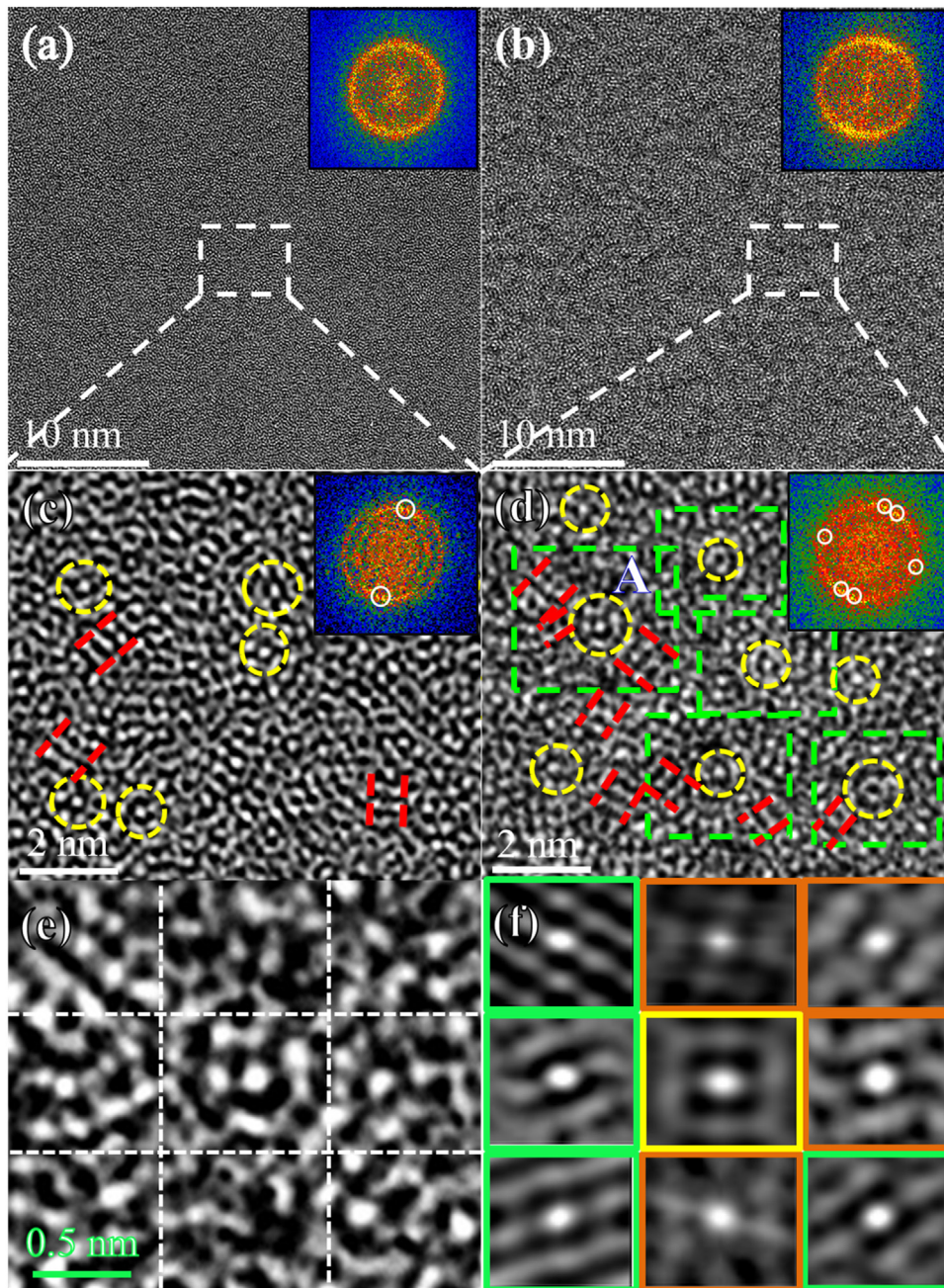
Fig. 8. The HRTEM images with the corresponding FFT pattern in the inset of (a) unfluxed $Fe_{39}Ni_{39}B_{12.82}Si_{2.75}Nb_{2.3}P_{4.13}$ BMG sample and (b) fluxed $Fe_{39}Ni_{39}B_{12.82}Si_{2.75}Nb_{2.3}P_{4.13}$ BMG sample, respectively, (c) and (d) are the enlarged images with the FFT patterns in the insets of the white square areas in (a) and (b), respectively, (e) the enlarged image of region A in (d), (f) the segmentation of the (e) for auto-correlation analysis.

the disappearance of nanospheres at the late stage of shear-band evolution. During shear-band evolution, the volumetric dilation is always accompanied, which may result in the dimension extension of nanospheres within the SB. With the further reduction of viscosity and increase in mobility caused by shear-induced structural disordering and generation of free volume, the coarsened nanospheres finally disappeared [69,70]. Besides, a sandwich-like heterogeneous structure inside the SBs is observed, as shown in Fig. 10c: a central dark region (II) is sandwiched by two bright regions (I). The regions I and II both remain fully glassy, as indicated by FFT patterns (see the insets of Fig. 10c). It has been reported that the heterogeneity structure in SBs is induced by the hierarchical volume dilatation, indicating a two-step plastic deformation mechanism in BMGs [26].

4. Discussion

It is known that SB initiates from a collection of shear transformation zone (STZ), which is associated with the cooperative shear motion of local events involving tens or hundreds of atoms [27]. Sarac et al. observed the similar FCC-FeNi nanocrystals in the $Fe_{50}Ni_{30}P_{13}C_7$ BMG, and suggested that these CLCs with lower shear modulus (or their interfaces) can act as sources and sinks for STZs [11]. The CLCs deformation can initiate STZs with similar atomic volumes; subsequently, the STZ is hindered by the homogenously distributed CLCs. Thus, the absorbed deformation can be widely spread through the regions of CLCs, then multiple SBs are expected to form. In our case, the abundant CLCs in the fluxed sample will provide much potential STZ sites, meanwhile, these CLCs
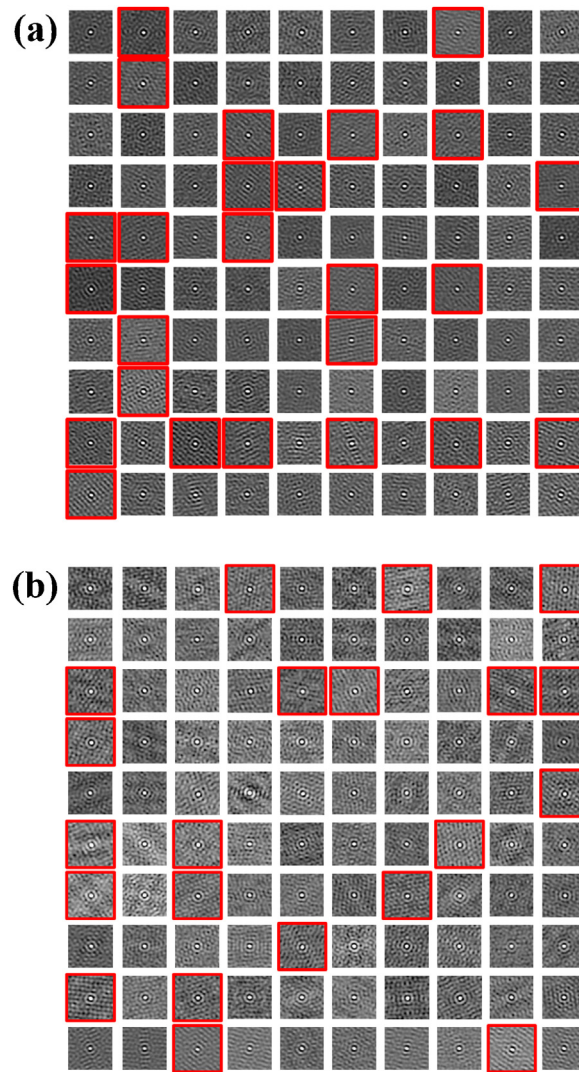
Fig. 9. The segmentation of HRTEM images of the unfluxed (a) and fluxed (b) $Fe_{39}Ni_{39}B_{12.82}Si_{2.75}Nb_{2.3}P_{4.13}$ BMG samples for auto-correlation analysis. The dimension of each segment or cell is 1.915×1.915 nm^2.

are spread around the high densely packed core of ILC (Fig. 8d), so that the embryonic SB initiated by CLCs can immediately be hindered by the around ILCs with high shear resistance [71], which preventing the full development of a single SB and its propagation.

Moreover, the phase separation takes place under compression loading due to the very small heat of mixing between Fe-Ni atomic pairs ($\triangle H$mix Fe-Ni = −2 kJ/mol) as compared to Fe-P, Fe-C, Ni-P, and Ni-C atomic pairs ($\triangle H$mix Fe-P = -39.5 kJ/mol, $\triangle H$mix Fe-C = −50 kJ/mol, $\triangle H$mix Ni-P = -34.5 kJ/mol, and $\triangle H$mix Ni-C = −39 kJ/mol, respectively) [72]. It should be emphasized that except for the very small heat of mixing between Fe-Ni atomic pairs, the heat of mixing between B and P atomic pairs is positive ($\triangle H$mix Ni-C = +0.5 kJ/mol [72]), and the atomic distributions of B and Si elements of this FeNi-based BMG was further modified with fluxing treatment as shown in Fig. 6b and c. Thus the joint effect of the heat of mixing between atomic pairs in the fluxed FeNi-based BMG sample stimulates phase separation under compression and further intensifies the heterogeneity of glassy structure. Areas with local stress concentrations induced by the elastic mismatch between two glassy phases upon loading can act as nucleation sites for SB, the harder of the two glassy phases should act to impede SB propagation. As SB propagation becomes more difficult, new SBs will initiate

in multiple orientations and contribute to plastic deformation and energy dispersion.

This multiscale deformation mechanism in the fluxed sample induced by the atomic- to nano-scales heterogeneity inhibits catastrophic failure and improves general plasticity. At atomic-scale, the unique "ILC surrounded by CLCs" structure of the fluxed sample provides fertile sites of STZs and the strong network structure, leading to the strong tendency to form multiple SBs. Then, the phase separation occurs under compression loading further promotes the multiplication and branching of SBs, functioning in the similar way as the unique atomic-scale structure, but on a nanometre scale. As a result, the multiplication and branching of SBs are actived, resulting in the pronounced plasticity of the fluxed sample. In addition, since the ILCs and nanospheres block the SB propagation during plastic deformation process, new SBs will be initiated at less favorable sites. Therefore, it is considered that the initiation of new SBs occurs at a higher stress, resulting in the strain-hardening phenomenon [73,74].

Except for the promoting proliferation and hindering propagation of SB, obtaining the stable SB evolution also benefits to the enhancement in plasticity and strength [75]. As indicated by the sandwich-like heterogeneity structure of SBs shown in Fig. 10c, a two-step evolution of SB involving different local structural varia-
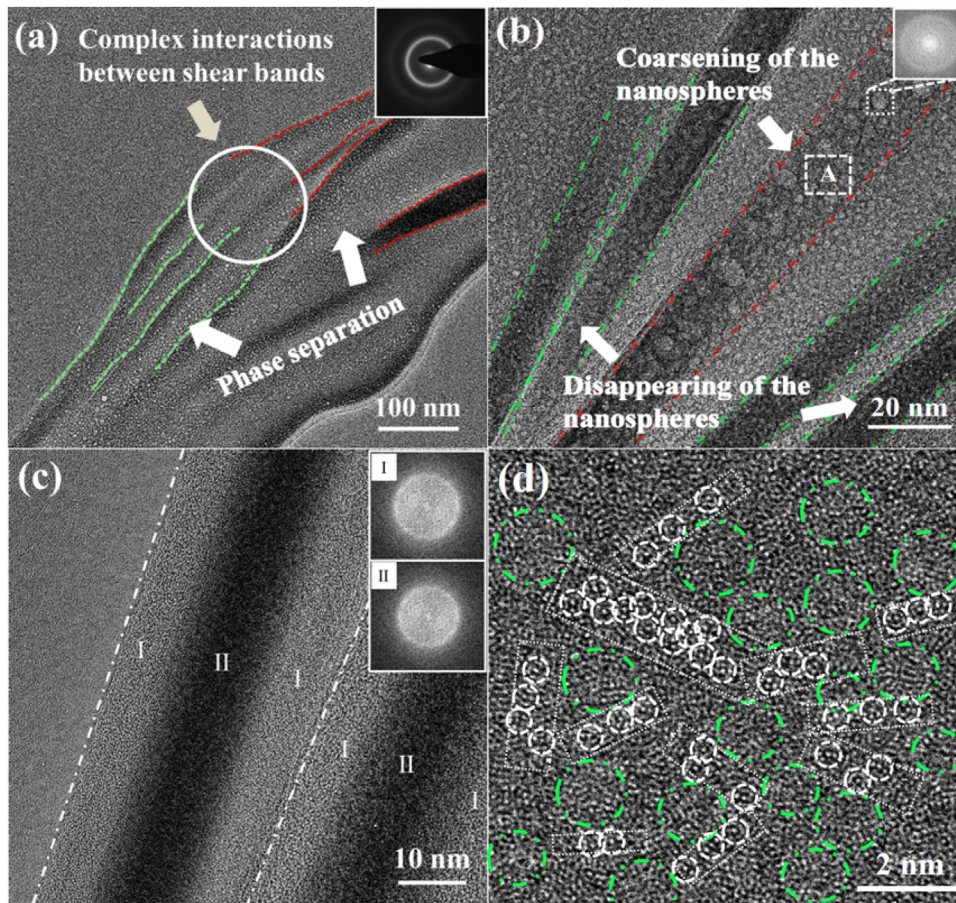
Fig. 10. (a) HRTEM image of fluxed $Fe_{39}Ni_{39}B_{12.82}Si_{2.75}Nb_{2.3}P_{4.13}$ BMG sample compressed uniaxial to a thin-disc shape (~30 % plastic strain), showing several SBs (red and green lines) and obvious phase separation, (b) the HRTEM image of compressed sample showing coarsening and disappearing of nanospheres in different regions of SBs, (c) the HRTEM image of SBs showing a sandwich-like heterogeneous structure, (d) the HRTEM image of high magnification of the white square area in (b) with green circles denoting the nanospheres and white squares showing the gathering of icosahedral-like clusters (white circles).

tion is suggested, including i) the rearrangement of atomic clusters, ii) the break of atomic bonds [26]. The i) step takes place when the deformation proceeds into plastic stage, the clusters in SBs would adjust their local positions, orientations, or shapes to accommodate the change of the local strain. The FCC-FeNi nanocrystals with "softer" metal-metal bonding nature will provide more freedom for bonds stretching and straining [11], while the high densely packed ILCs may limit the flexibility of deformation among clusters [71]. This can be verified by the coarsening of nanospheres, the decrease of nanocrystals, and the position change of icosahedral-like clusters in SB (Fig. 10b). For more clarity, the selected area A of Fig. 10b is enlarged as shown in Fig. 10d, in which the nanospheres and the space between them are marked by green circles and white rectangles, respectively. As shown in the figure, compared with the as-cast sample (Fig. 8b), the number of CLCs decreases and the ILCs gather together in the space between these nanospheres during the evolution of SBs. It can be therefore suggested that, during the i) step of plastic deformation, the CLCs and nanospheres become loosely packed, inducing the volume dilatation of them, while the ILCs still act as an entity to response to the local stress but change their position. This evolution of atomic-scale structure in SB releases the stress concentration, and improves the stability of SB.

As local stress further increases, atomic clusters gradually lose their coordinated atoms and become unstable, then the ii) step occurs. Since the rearrangement of atomic clusters cannot sustain the increased stress, the bonds inside the clusters would break, and then quickly extend their dimension, forming a liquid-like morphology as shown in region II of Fig. 10c. This liquid-like region II

would incubate nanovoids or micro-cracks, and even cause the final fracture along the pre-sheared path (region I) [26]. In the fluxed sample, the ii) step will be effectively retard by the unique atomic-scale structure. Fig. 11a shows the HRTEM image of a SB at the initial stage of forming sandwich-like structure. As shown in the figure, the phase separation is disappeared and an inhomogeneous structure with bright and dark areas can be observed within the SB. The enlarged region A in Fig. 11a is shown in Fig. 11b. It can be seen that these bright areas connecting a network are consist of ILCs (marked by yellow circles), while the dark area exhibits disordering structure. Since the stable ILCs are hard to break [76], the higher energy is needed for fluxed sample with more ILCs to fail, then further delays the development from SBs into cracks. The fully break of nanospheres and CLCs at ii) step, together with the strengthened "backbones" of ILCs, can help to offset shear-softening and providing a stable evolution of SB, thereby resulting in the improved the strength and the overall plastic deformability of the fluxed FeNi-based BMG.

The clusters with various structural characteristics in fluxed sample participate in the deformation process with different responses. Based on the above analysis, we can conclude that the origin of enhanced plasticity in the fluxed sample is based on the following two reasons: Firstly, the "ILC surrounded by CLCs" structure in this FeNi-based BMG and the phase separation during deformation lead to the multiscale heterogeneity, resulting in the strong interactions of multiple SBs. Secondly, the unique atomic-scale clusters in the fluxed FeNi-based BMG sample effectively stimulates more areas to deform in the i) step of shear-band
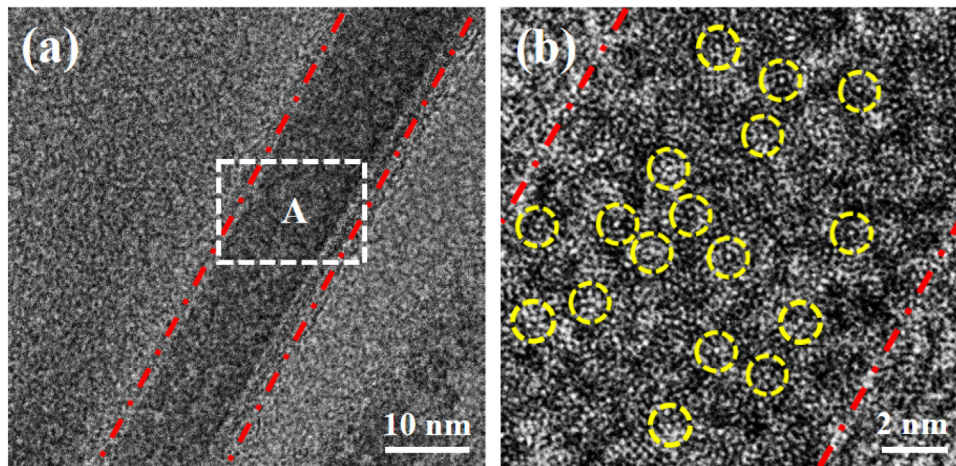
Fig. 11. (a) HRTEM image of SB at the initial stage of forming sandwich-like structure; (b) Enlarged region A in (a), yellow circle represent the icosahedral-like clusters.

evolution, and at the same time retard the ii) step plastic deformation process, resulting in a stable evolution process from SBs to cracks, thereby the improved overall plasticity. While the enhanced strength can be attributed to the phase separation and the existence of more ILCs in the fluxed sample, which lead to continuous strain-hardening and high resistance for shear expansion.

5. Conclusion

In summary, by using the fluxing technique, a ductile $Fe_{39}Ni_{39}B_{12.82}Si_{2.75}Nb_{2.3}P_{4.13}$ BMG with large plastic strain over 50 % and superhigh compression strength of 4220 MPa were successfully developed. The combination of extraordinary plasticity and superhigh strength is a breakthrough in a general trade-off between ε_p and σ_c of the Fe-based BMG family. Also, the origin of enhanced plasticity and strength of this FeNi-based BMG upon fluxing treatment were investigated in detail. It is found that no obvious chemical inhomogeneity occurs, but the atomic-scale structure changes with fluxing treatment. More FCC-FeNi nanocrystals and icosahedral-like atomic clusters in the fluxed FeNi-based BMG sample lead to the increase of heterogeneity in the short-range scale, while their uniform distribution results in more disordering degree in the medium-range scale. It is worth mentioning that the ILCs in the fluxed sample are usually surrounded by several nanocrystals, and homogeneously distributed throughout the alloy. Furthermore, phase separation during deformation and a sandwich-like heterogeneous structure of SB were observed. The unique atomic-scale structure of fluxed sample and the phase separation occuring during deformation generates more potential STZ sites and leads a stable evolution process of SB, resulting in the strong interactions of multiple SBs, thereby the simultaneous improvement of plasticity and strength. This study gives us a guideline to develop plastic Fe-based BMGs with superhigh strength for the potential application of commercial materials in the near future.

Acknowledgments

References

[1] W.H. Wang, C. Dong, C.H. Shek, Mater. Sci. Eng. R 44 (2004) 45–89.
[2] J.J. Lewandowski, W.H. Wang, A.L. Greer, Philos. Mag. Lett. 85 (2005) 77–87.
[3] P. Yu, H.Y. Bai, Mater. Sci. Eng. A 485 (2008) 1–4.
[4] D.C. Hofmann, J.Y. Suh, A. Wiest, G. Duan, M.L. Lind, M.D. Demetriou, W.L. Johnson, Nature 451 (2008) 1085–1090.
[5] J. Fan, W. Rao, J.W. Qiao, P.K. Liaw, D. Sopu, D. Kiener, J. Eckert, G.Z. Kang, Y.C. Wu, J. Mater. Sci. Technol. 50 (2020) 192–203.
[6] S. Scudino, B. Jerliu, S. Pauly, K. Surreddi, U. Kühn, J. Eckert, Scr. Mater. 65 (2011) 815–818.
[7] S.V. Ketov, Y.H. Sun, S. Nachum, Z. Lu, A. Checchi, A.R. Beraldin, H.Y. Bai, W.H. Wang, D.V. Louzguine-Luzgin, M.A. Carpenter, A.L. Greer, Nature 524 (2015) 200–203.
[8] C. Ebner, B. Escher, C. Gammer, J. Eckert, S. Pauly, C. Rentenberger, Acta Mater. 160 (2018) 147–157.
[9] X.H. Ma, X.H. Yang, Q. Li, S.F. Guo, J. Alloys Compd. 577 (2013) 345–350.
[10] W.M. Yang, H.S. Liu, Y.C. Zhao, A. Inoue, K.M. Jiang, J.T. Huo, H.B. Ling, Q. Li, B.L. Shen, Sci. Rep. 4 (2014) 6233.
[11] B. Sarac, Y.P. Ivanov, A. Chuvilin, T. Schöberl, M. Stoica, Z. Zhang, J. Eckert, Nat. Commun. 9 (2018) 1333.
[12] S.F. Guo, J.L. Qiu, P. Yu, S.H. Xie, W. Chen, Appl. Phys. Lett. 105 (2014), 161901.
[13] H.K. Kim, M. Lee, K.R. Lee, J.C. Lee, Acta Mater. 61 (2013) 6597–6608.
[14] H.K. Kim, J.P. Ahn, B.J. Lee, K.W. Park, J.C. Lee, Acta Mater. 157 (2018) 209–217.
[15] Q.Q. Wang, J. Zhou, Q.S. Zeng, G.L. Zhang, K.B. Yin, T. Liang, W.M. Yang, M. Stoica, L.T. Sun, B.L. Shen, Materialia 9 (2020), 100561.
[16] J. Schroers, W.L. Johnson, Phys. Rev. Lett. 93 (2004), 255506.
[17] M.D. Demetriou, M. Floyd, C. Crewdson, J.P. Schramm, G. Garrett, W.L. Johnson, Scr. Mater. 65 (2011) 799–802.
[18] M.D. Demetriou, M.E. Launey, G. Garrett, J.P. Schramm, D.C. Hofmann, W.L. Johnson, R.O. Ritchie, Nat. Mater. 10 (2011) 123–128.
[19] N. Chen, D. Pan, D.V. Louzguine-Luzgin, G.Q. Xie, M.W. Chen, A. Inoue, Scr. Mater. 62 (2010) 17–20.
[20] N. Chen, L. Gu, G.Q. Xie, D.V. Louzguine-Luzgin, A.R. Yavari, G. Vaughan, S.D. Imhoff, J.H. Perepezko, T. Abe, A. Inoue, Acta Mater. 58 (2010) 5887–5897.
[21] D. Granata, E. Fischer, V. Wessels, J.F. Löffler, Acta Mater. 71 (2014) 145–152.
[22] D. Granata, E. Fischer, V. Wessels, J. Löffler, Appl. Phys. Lett. 106 (2015), 011902.
[23] M. Floyd, M.D. Demetriou, W.L. Johnson, Scr. Mater. 146 (2018) 312–315.
[24] W.M. Yang, C. Wan, H.S. Liu, Q. Li, Q.Q. Wang, H. Li, J. Zhou, L. Xue, B.L. Shen, A. Inoue, Mater. Des. 129 (2017) 63–68.
[25] Y.F. Shi, M.L. Falk, Acta Mater. 55 (2007) 4317–4324.
[26] Y. Shao, K.F. Yao, M. Li, X. Liu, Appl. Phys. Lett. 103 (2013), 171901.
[27] A.L. Greer, Y.Q. Cheng, E. Ma, Mater. Sci. Eng. R 74 (2013) 71–132.
[28] H. Guo, C.B. Jiang, B.J. Yang, J.Q. Wang, J. Mater. Sci. Technol. 33 (2017) 1272–1277.
[29] J. Zhou, Q.Q. Wang, X.D. Hui, Q.S. Zeng, Y.W. Xiong, K.B. Yin, B.A. Sun, L.T. Sun, M. Stoica, W.H. Wang, B.L. Shen, Mater. Des. 191 (2020), 108597.
[30] A.P. Hammersley, S.O. Svensson, M. Hanfland, A.N. Fitch, D. Hausermann, High Press. Res. 14 (1996) 235–248.
[31] I.K. Jeong, J. Thompson, Th. Proffen, A. Perez, S.J.L. Billinge, J. Appl. Cryst. 34 (2001) 536.
[32] G.N. Yang, S.Q. Chen, J.L. Gu, S.F. Zhao, J.F. Li, Y. Shao, H. Wang, K.F. Yao, Philos. Mag. 96 (2016) 2243–2255.
[33] H.C. Sun, Z.L. Ning, J.L. Ren, W.Z. Liang, Y.J. Huang, J.F. Sun, X. Xue, G. Wang, J. Mater. Sci. Technol. 35 (2019) 2079–2085.
[34] M. Kumar, E. Nicholson, D.W. Kirk, S.J. Thorpe, C.V. Singh, J. Alloys Compd. 787 (2019) 840–850.

[35] D. Sopu, C. Soyarslan, B. Sarac, S. Bargmann, M. Stoica, J. Eckert, Acta Mater. 106 (2016) 199–207.
[36] R.T. Qu, Z.F. Zhang,J. Appl. Phys. 114 (2013), 193504.
[37] A. Inoue, B.L. Shen, C.T. Chang, Acta Mater. 52 (2004) 4093–4099.
[38] K.F. Yao, C.Q. Zhang, Appl. Phys. Lett. 90 (2007) 61901.
[39] A. Inoue, T. Zhang, A. Takeuchi, Appl. Phys. Lett. 71 (1997) 464–466.
[40] A. Inoue, B.L. Shen, A.R. Yavari, A.L. Greer, J. Mater. Res. 18 (2003) 1487–1492.
[41] Z.P. Lu, C.T. Liu, J.R. Thompson, W.D. Porter,Phys. Rev. Lett. 92 (2004), 245503.
[42] K. Amiya, A. Urata, N. Nishiyama, A. Inoue, Mater. Trans. 45 (2004) 1214–1218.
[43] J. Shen, Q.J. Chen, J.F. Sun, H.B. Fan, G. Wang,Appl. Phys. Lett. 86 (2005), 151907.
[44] X.J. Gu, A.G. McDermott, S.J. Poon, G.J. Shiflet,Appl. Phys. Lett. 88 (2006), 211905.
[45] T. Zhang, F.J. Liu, S.J. Pang, R. Li, Mater. Trans. 48 (2007) 1157–1160.
[46] D.H. Kim, J.M. Park, D.H. Kim, W.T. Kim, J. Mater. Res. 22 (2007) 471–477.
[47] F.J. Liu, Q.W. Yang, S.J. Pang, C.L. Ma, T. Zhang, Mater. Trans. 45 (2008) 231–234.
[48] X.J. Gu, S.J. Poon, G.J. Shiflet, M. Widom, Acta Mater. 56 (2008) 88–94.
[49] J.H. Yao, J.Q. Wang, Y. Li,Appl. Phys. Lett. 92 (2008), 251906.
[50] Z.Y. Chang, X.M. Huang, L.Y. Chen, M.Y. Ge, Q.K. Jiang, X.P. Nie, J.Z. Jiang, Mater. Sci. Eng. A 517 (2009) 246–248.
[51] S.F. Guo, L. Liu, N. Li, Y. Li, Scr. Mater. 62 (2010) 329–332.
[52] S.F. Guo, N. Li, C. Zhang, L. Liu, J. Alloys Compd. 504 (2010) S78–S81.
[53] P. Ramasamy, M. Stoica, S. Bera, M. Calin, J. Eckert, J. Alloys Compd. 707 (2017) 78–81.
[54] J. Zhou, B.A. Sun, Q.Q. Wang, Q.M. Yang, W.M. Yang, B.L. Shen, J. Alloys Compd. 783 (2019) 555–564.
[55] X.H. Yang, X.H. Ma, Q. Li, S.F. Guo, J. Alloys Compd. 554 (2013) 446–449.
[56] J. Shin, S. Yi, K.G. Pradeep, P.P. Choi, D. Raabe, J. Mater. Res. 23 (2013) 190–193.
[57] Z.M. Li, F. Körmann, B. Grabowski, J. Neugebauer, D. Raabe, Acta Mater. 136 (2017) 262–270.
[58] C.C. Yuan, Z.W. Lv, C.M. Pang, X.L. Wu, S. Lan, C.Y. Lu, L.G. Wang, H.B. Yu, J.H. Luan, W.W. Zhu, G.L. Zhang, Q. Liu, X.L. Wang, B.L. Shen, J. Alloys Compd. 798 (2019) 517–522.
[59] H.W. Sheng, W.K. Luo, F.M. Alamgir, J.M. Bai, E. Ma, Nature 439 (2006) 419–425.
[60] A.H. Taghvaei, M. Stoica, K.G. Prashanth, J. Eckert, Acta Mater. 61 (2013) 6609–6621.
[61] T. Takagi, T. Ohkubo, Y. Hirotsu, B.S. Murty, K. Hono, D. Shindo, Appl. Phys. Lett. 79 (2001) 485.
[62] J. Saida, M. Matsushita, A. Inoue, Appl. Phys. Lett. 79 (2001) 412.
[63] W.K. Luo, H.W. Sheng, F.M. Alamgir, J.M. Bai, J.H. He, E. Ma,Phys. Rev. Lett. 92 (2004), 145502.
[64] Q. Wang, C.T. Liu, Y. Yang, Y.D. Dong, J. Lu,Phys. Rev. Lett. 106 (2011), 215505.
[65] J. Hwang, Z.H. Melgarejo, Y.E. Kalay, I. Kalay, M.J. Kramer, D.S. Stone, P.M. Voyles,Phys. Rev. Lett. 108 (2012), 195505.
[66] H.J. Goldschmidt, Metallurgia 40 (1949) 103.
[67] J.M. Liang, L.J. Chen, Appl. Phys. Lett. 64 (1994) 1224.
[68] X.J. Liu, G.L. Chen, H.Y. Hou, X. Hui, K.F. Yao, Z.P. Lu, C.T. Liu, Acta Mater. 56 (2008) 2760–2769.
[69] J. He, I. Kaban, N. Mattern, K. Song, B.A. Sun, J.Z. Zhao, D.H. Kim, J. Eckert, A.L. Greer, Sci. Rep. 6 (2016) 25832.
[70] M.D. Demetriou, W.L. Johnson, J. Appl. Phys. 95 (2004) 2857–2865.
[71] O. Adjaoud, K. Albe, Acta Mater. 168 (2019) 393–400.
[72] A. Takeuchi, A. Inoue, Mater. Trans. 46 (2005) 2817–2829.
[73] L.J. Wu, Z.W. Zhu, D.M. Liu, H.M. Fu, H. Li, A.M. Wang, H.W. Zhang, Z.K. Li, L. Zhang, H.F. Zhang, J. Mater. Sci. Technol. 37 (2020) 64–70.
[74] T. Wang, J.J. Si, Y.D. Wu, K. Lv, Y.H. Liu, X.D. Hui, Scr. Mater. 150 (2018) 106–109.
[75] Y.C. Wang, X.M. Luo, L.J. Chen, H.W. Yang, B. Zhang, G.P. Zhang, J. Mater. Sci. Technol. 34 (2018) 2283–2289.
[76] Y.Q. Cheng, E. Ma, Prog. Mater. Sci. 56 (2011) 379–473.